RESEARCH PAPER

^{99m}Tc-labeled anionic linear-globular dendrimers conjugated with l-arginine as a novel radiotracer for single photon emission computed tomography of breast tumor xenografts

Parham Karimi [1], Mehdi Shafiee Ardestani [1, 2*], Massoud Amanlou [3], Tahereh Zadeh Mehrizi [4*], Mehdi Mirzaei [5], Ahmad Javanmard [6], Seyed Mohsen Asghari [7]

[1] Department of Radiopharmacy, Faculty of Pharmacy, Tehran University of Medical Sciences, Tehran, Iran
[2] Research Center for Nuclear Medicine, Shariati Hospital, Tehran, Iran
[3] Department of Medicinal Chemistry, Faculty of Pharmacy, Tehran University of Medical Sciences, Tehran, Iran
[4] Health Management and Economics Research Center, Health Management Research Institute, Iran University of Medical Sciences, Tehran, Iran
[5] Ministry of Health and Medical Education, Tehran, Iran
[6] Student Research Committee, Cancer Research Center, Shahid Beheshti University of Medical Sciences, Tehran, Iran
[7] Department of Biochemistry, Institute of Biochemistry and Biophysics, University of Tehran, Tehran, Iran

ABSTRACT

Objective(s): Dendrimers are promising molecular imaging platforms because of their multivalency and tunable surfaces. This study synthesized a PEGylated anionic linear-globular dendrimer conjugated with L-arginine and labeled with technetium-99m (^{99m}Tc-DND-G2-Arg) as a targeted SPECT tracer for breast cancer.

Materials and Methods: G2-dendrimers were synthesized via divergent esterification and conjugated to L-arginine using carbodiimide chemistry. Physicochemical characterization was performed using FTIR, FE-SEM, DLS, and LC-MS. Cell compatibility was assessed by MTT assay in Vero cells. Radiochemical purity/stability were assessed by radio thin layer chromatography. In vivo biodistribution and SPECT imaging were conducted at 5, 30, and 120 minutes post-injection in BALB/c mice with 4T1 tumors. Kinetic behavior was analyzed using a two-compartment model.

Results: FTIR and LC-MS analyses verified successful L-arginine conjugation to G2-PEG-citrate-ALGD. The spherical nanoparticles (FE-SEM: 134.91 ± 15.01 nm; DLS: 202.4 nm; zeta potential: -7.3 mV) exhibited excellent cytocompatibility (>95% viability). The highly pure radiolabeled conjugate (99.68%) also remained stable, exceeding 95% over the physical half-life and retaining 80-85% stability at 48 hours in PBS and serum. In vivo studies revealed specific tumor uptake (0.87 ± 0.19 %ID/g), which decreased by 31% after L-arginine blocking ($p < 0.05$). SPECT imaging demonstrated a strong early tumor uptake (SUVmax 4.8 at 30 min) with rapid blood clearance, while kinetic modeling indicated fast tumor influx, efficient irreversible trapping, and minimal efflux.

Conclusion: ^{99m}Tc-DND-G2-Arg demonstrates specific tumor targeting, favorable pharmacokinetics, and excellent in vivo stability in a preclinical xenograft model, supporting further investigation as a potential SPECT radiotracer for imaging arginine-enriched breast cancers.

Keywords: *Technetium; Dendrimers; Arginine; Radionuclide imaging; Breast neoplasms*

How to cite this article

Karimi P, Shafiee Ardestani M, Amanlou M, Zadeh Mehrizi T, Mirzaei M, Javanmard A, Asghari SM. ^{99m}Tc-labeled anionic linear-globular dendrimers conjugated with L-arginine as a novel radiotracer for single photon emission computed tomography of breast tumor xenografts. Nanomed J. 2026; 13: 1-.

DOI: 10.22038/nmj.2026.96242.2436

* *Corresponding author(s):* **Mehdi Shafiee Ardestani**, Associate Professor, Department of Radiopharmacy, Faculty of Pharmacy, Tehran University of Medical Sciences, Tehran, Iran. Phone: +982164122103, Email: *shafieeardestani@gmail.com*. **Tahereh Zadeh Mehrizi**, Assistant Professor, Ministry of Health and Medical Education, Tehran, Iran. Phone: +982188782919, Email: *Mehrizi.t@iums.ac.ir*; *taherehzadehmehrizi@gmail.com*.

Note. This manuscript was submitted on June 05, 2026; approved on August 25, 2026.

GRAPHICAL ABSTRACT

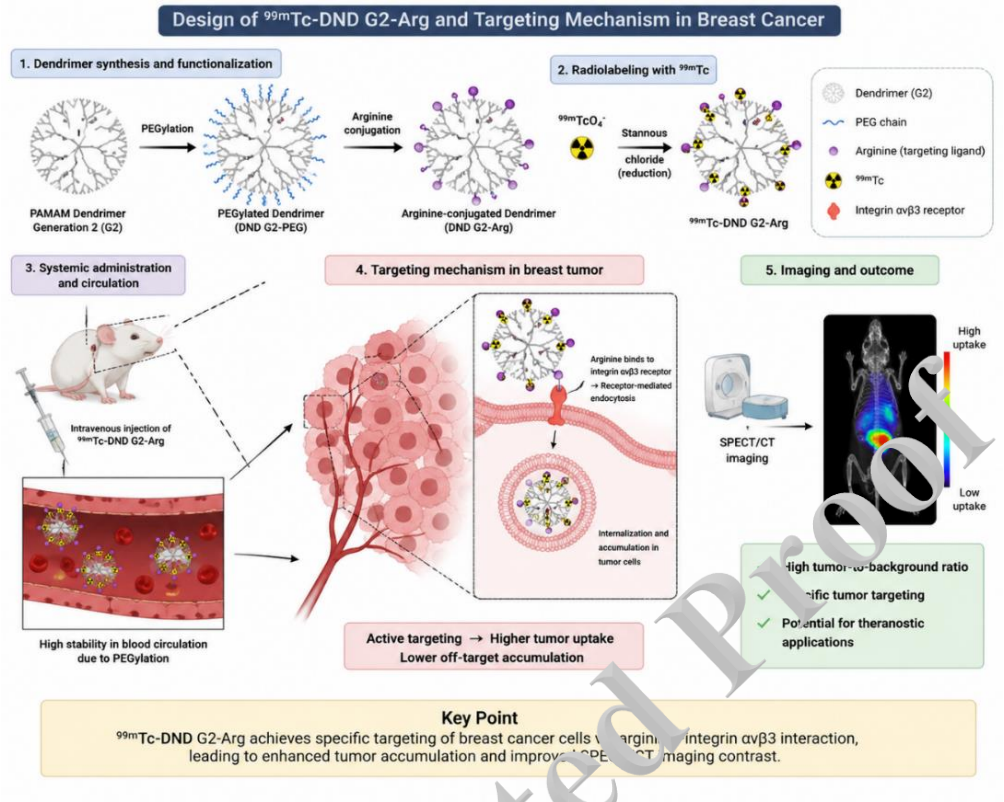

INTRODUCTION

Breast cancer remains the most commonly diagnosed malignancy and the leading cause of cancer-related death among women worldwide [1]. According to the World Health Organization, breast cancer accounts for approximately one-quarter of all cancers diagnosed in women, making it a major contributor to the global cancer burden [2]. The Global Cancer Observatory reported more than 2.3 million new cases and 685,000 deaths worldwide in 2020, highlighting the urgent need for improved strategies for early diagnosis and accurate disease stratification [3]. Early diagnosis at a localized stage is strongly associated with improved survival, less intensive treatment, and better quality of life [4, 5]. These findings emphasize the critical role of accurate imaging modalities in the management of breast cancer.

Despite substantial advances in diagnostic imaging, current modalities still have important limitations. While mammography is the most widely used imaging modality for breast cancer, its sensitivity declines in women with dense breasts, and it has limited ability to detect biologically aggressive or non-calcified lesions [6]. Magnetic Resonance Imaging (MRI) is highly sensitive, but is costly and time-consuming [7, 8]. Ultrasound is widely available; however, it is highly operator-dependent and associated with relatively high false-positive rates [9]. Although Molecular imaging techniques like PET and PET/CT provide excellent sensitivity, they are unsuitable for routine screening because of their high cost, limited availability, and reliance on expensive short-lived radionuclides [10, 11].

Single-photon emission computed tomography (SPECT) is a widely available molecular imaging modality capable of detecting functional and metabolic alterations associated with tumor development [12]. Among SPECT radionuclides, technetium-99m (^{99m}Tc) remains the radionuclide of choice in the clinic owing to its highly favorable physical characteristics, such as a short half-life, optimal gamma-ray energy, and availability through generator systems [13, 14]. Nevertheless, the majority of the traditional ^{99m}Tc-labeled agents are limited by low tumor specificity, rapid clearance, and unfavorable tumor-to-background ratios [15, 16]. These

limitations have driven the development of nanotechnology-based platforms designed to improve radiotracer targeting and delivery [13, 17, 18].

Dendrimer-based nanoradiotracers are attractive molecular imaging platforms because of their well-defined structure, nanometric size, and high density of modifiable surface functional groups [19, 20]. Dendrimers provide precise control over size, charge, and surface properties, facilitating efficient conjugation of targeting ligands and radionuclides [21]. Anionic linear-globular dendrimers (ALGD), composed of biocompatible building blocks like citric acid and polyethylene glycol (PEG), offer additional advantages, including low toxicity, high aqueous solubility, and desirable biodistribution properties [22-30]. Generation 2 (G2) dendrimers achieve an optimal balance between molecular size and biological performance, promoting tumor penetration while minimizing reticuloendothelial system (RES) uptake [31]. PEGylation further prolongs circulation time and reduces immunogenicity, making these dendrimers attractive platforms for in vivo imaging [32].

Targeted molecular imaging can be further enhanced by incorporating biologically relevant ligands. L-arginine, a semiessential amino acid, plays a role in tumor metabolism and cell proliferation [33]. Breast cancer and several other tumor types overexpress cationic amino acid transporters to facilitate an increased uptake of arginine [34, 35]. This metabolic characteristic provides a strong rationale for exploiting L-arginine as a targeting agent. Accordingly, conjugation of L-arginine to dendrimers may promote preferential tumor accumulation through transporter-mediated uptake [33, 36, 37].

Therefore, this study aimed to develop and characterize a novel ^{99m}Tc-labeled PEG-citrate anionic linear-globular dendrimer conjugated with L-arginine (^{99m}Tc-DND-G2-Arg) as a potential targeted SPECT imaging agent. We further evaluated its tumor-targeting capability and imaging performance in a breast cancer xenograft model.

MATERIALS AND METHODS

Materials

The following materials were used in this study: dicarboxylated polyethylene glycol 600 Da (PEG-600; Merck, Germany); Sodium citrate ($Na_3C_6H_5O_7$; Merck, Germany); L-arginine ($C_6H_{14}N_4O_2$, purity ≥98%, Merck, Germany); 1-ethyl-3-(3-dimethylaminopropyl) carbodiimide hydrochloride (EDC; Sigma-Aldrich, USA); N-hydroxysuccinimide (NHS; Sigma-Aldrich, USA); dimethyl sulfoxide (DMSO; Merck, Germany); dimethylformamide (DMF) (Merck, Germany); Methanol and absolute ethanol (≥99.9%, Zagros Company, Iran); N, N'-dicyclohexylcarbodiimide (DCC; Sigma-Aldrich, USA); Phosphate-buffered saline (PBS, pH 7.4; Atlas Teb, Iran); Dialysis membranes with a molecular weight cut-off (MWCO) of 1000-3000 Da (Thermo Fisher Scientific, USA); Potassium bromide (KBr) (Merck, Germany); Uranyl acetate and phosphotungstic acid (Sigma-Aldrich, USA); silica gel 60 F_{254} aluminum sheets (Merck, Germany) and Whatman No. 1 chromatography paper (Scientific laboratory supplies, England); C18 reversed-phase columns (Agilent Technologies, USA). Freshly eluted ^{99m}Tc-pertechnetate ($^{99m}TcO_4^-$) was obtained from a ^{99}Mo/^{99m}Tc generator (Pars Isotope, Iran) using normal saline. Stannous chloride dihydrate ($SnCl_2{\cdot}2H_2O$) (Merck, Germany) was used as the reducing agent for ^{99m}Tc labeling of the dendrimer conjugate.

Synthesis of G2-PEG-citrate-ALGD

G2-PEG-citrate anionic linear-globular dendrimers (G2-PEG-citrate-ALGD) were synthesized using a divergent growth method, as previously described with minor modifications [38, 39]. In brief, 2 mL of PEG-600 (1.67 mmol) was dissolved in 5 mL of DMF containing 200 mg of $CaCl_2$ as a dehydrating agent. The solution was stirred for 15 min at room temperature at 400 rpm. Subsequently, 150 mg (0.6 mmol) of DCC and 150 mg of citric acid were added to the reaction mixture, which was stirred at 400 rpm for 1 hour to activate the carboxyl groups and facilitate esterification for the formation of the first-generation dendrimer. To synthesize the second-generation dendrimer, 225 mg (0.9 mmol) of DCC and 200 mg of citric acid were added to the reaction mixture. The reaction was maintained at room temperature with continuous stirring (400 rpm) for 7 days.

Conjugation of G2-PEG-citrate-ALGD with L-Arginine

L-arginine was conjugated to the surface of the G2 dendrimer using carbodiimide-mediated EDC/NHS coupling to form stable amide bonds. The purified G2 dendrimers were dissolved in 5 mL of distilled water and manually stirred for 5 min. The solution was filtered through filter paper, and the filtered solution was concentrated by rotary evaporation at 100 °C for 30 min to

reduce its volume. Subsequently, 1 to 3 mL of DMF was added to the concentrated dendrimer solution to improve the solubility of hydrophobic components. After stirring, DCC (150 mg) and EDC (30 mg) were added, and the activation reaction was allowed to proceed at room temperature (400 rpm) for 15 min to activate the terminal carboxyl and amine groups of the dendrimer. Subsequently, 500 mg of solid L-arginine was added to the activated dendrimer solution, and the conjugation reaction was continued at room temperature with continuous stirring at 400 rpm for 7 days. For purification, the final conjugate was filtered through filter paper to remove insoluble impurities and unreacted reagents. The filtrate was then dialyzed against distilled water using a 2000 Da MWCO membrane for 48 hours to remove unbound L-arginine and residual coupling reagents. The purified product was then lyophilized and stored at 4 °C until further characterization and radiolabeling experiments.

Characterization techniques

Fourier Transform Infrared (FTIR) spectroscopy

FTIR analysis was performed to confirm the successful synthesis of G2 dendrimer, PEGylation, and L-arginine conjugation. Approximately 2 mg of the lyophilized dendrimer conjugate was thoroughly mixed with 200 mg of dry KBr and compressed into transparent pellets using a hydraulic press. FTIR spectra were recorded in the range of 400–4000 cm^{-1} with a resolution of 4 cm^{-1} using an AVATAR FTIR spectrometer (Thermo Fisher Scientific, USA).

Field Emission Scanning Electron Microscopy (FE-SEM)

Surface morphology and particle size distribution of the synthesized dendrimer conjugate were characterized using FE-SEM. A dilute aqueous solution of the conjugate was dropwise cast onto a clean silicon wafer and air-dried at room temperature. The sample was coated with a thin (~3 nm) gold layer to enhance electrical conductivity. Imaging was performed using a MIRA II FE-SEM (TESCAN, Czech Republic) with an accelerating voltage of 15 to 20 kV. The particle size distribution was determined by measuring at least 100 particles from multiple micrographs.

Dynamic Light Scattering (DLS) and Zeta Potential Analysis

Hydrodynamic diameter, size distribution, polydispersity index (PDI), and colloidal stability of the dendrimer conjugate were determined by DLS. Zeta potential measurements were performed to evaluate the surface charge and predict long-term stability. Samples were prepared by dispersing the lyophilized conjugate in PBS (pH 7.4) at a concentration of 0.1 mg/mL and filtering the suspension through a 0.22 µm membrane filter. Measurements were performed at 25°C using a SZ-100 nanoparticle analyzer (Horiba, Japan) with a scattering angle of 90°. Each measurement was performed in triplicate.

Liquid Chromatography-Mass Spectrometry (LC-MS)

The molecular weight and purity of the synthesized conjugate were confirmed by LC-MS analysis. Analyses were performed using an Agilent 1290 Infinity LC system connected to a 6230 Time-of-Flight (TOF) mass spectrometer (Agilent Technologies, USA). Chromatographic separation was performed on a C18 reversed-phase column (2.1 × 100 mm, 1.7 µm particle size) at 40 °C. The mobile phase consisted of (A) water with 0.1% formic acid and (B) acetonitrile with 0.1% formic acid. A linear gradient from 5% to 95% B was applied over 20 min at a flow rate of 0.3 mL/min. The injection volume was 5 to 10 µL. Electrospray ionization was performed in both positive and negative modes. Mass spectra were acquired over an m/z range of 100 to 3000 Da. Source parameters included a drying gas temperature of 300°C, a drying gas flow rate of 8 L/min, and a capillary voltage of 3500 V. Data collection and analysis were performed using MassHunter software.

Cell culture

The 4T1 mouse mammary carcinoma and Vero cells were obtained from the Pasteur Institute (Tehran, Iran). Cells were cultured in RPMI 1640 medium containing 10% fetal bovine serum (FBS), 100 units/mL penicillin, and 100 µg/mL streptomycin at 37°C in a humidified atmosphere containing 5% CO_2.

In vitro cytotoxicity assay

The cytotoxicity of the dendrimer conjugate was assessed using the MTT assay. Vero cells were seeded in 96-well plates at a density of 1 × 10^4 cells/well and allowed to attach for 24 h. The medium was then replaced with fresh medium containing the conjugate at concentrations of 0, 7.8, 15.6, 31.3, 62.5, 125, 250, and 500 µg/mL and incubated for 24 h. Untreated cells and cells treated with 0.1% Triton X-100 served as negative and positive controls, respectively. After incubation, MTT solution (5 mg/mL in PBS) was added, and the plates were incubated for a further 4 h. Formazan crystals were dissolved in

DMSO, and the absorbance was measured at 570 nm using an ELISA reader (BioTek; USA). Experiments were performed in triplicate. The half-maximal inhibitory concentration (IC_{50}) was determined using nonlinear regression analysis.

Radiolabeling with technetium-99m

Radiolabeling of the conjugates with ^{99m}Tc was performed using the stannous chloride reduction method [40]. Briefly, 50 mCi (1.85 GBq) of freshly eluted ^{99m}Tc-pertechnetate ($^{99m}TcO_4^-$) in 0.5 mL of normal saline was reduced by adding 70 µL of stannous chloride solution ($SnCl_2{\cdot}2H_2O$, 2 mg/mL in 0.1 M HCl) and incubated for 10 min at room temperature. The pH of the solution was adjusted to approximately 8 using citrate buffer (0.1 M, pH 8). Subsequently, 100 µL of G2-PEG-citrate-ALGD-L-arginine solution (1 mg/mL in PBS) was added to the reduced ^{99m}Tc solution and incubated for 10 min at room temperature with gentle shaking to allow radiolabeling.

Radiochemical purity and stability assessment

The radiochemical purity (RCP) of the ^{99m}Tc-labeled conjugate was determined by instant thin-layer chromatography (ITLC) using silica gel impregnated fiberglass plates (ITLC-SG, Agilent Technologies) as the stationary phase and acetone and normal saline as the mobile phase. A 2 to 5 µL aliquot of the labeled product was applied 1 cm above the lower edge of the ITLC strip and developed in the corresponding mobile phase. After development, the strips were air-dried, cut into 1 cm pieces, and counted in a gamma counter (Dewaid, Iran). The radiochemical purity was calculated as the percentage of radioactivity associated with the radiolabeled conjugate relative to the total radioactivity. As an alternative method, an RTLC scanner (RTLC 2419, Pasargad Process Control Company, Iran) was used for direct scanning and quantification.

To evaluate the radiochemical stability of the ^{99m}Tc-DND-G2-Arg complex under quasi-physiological conditions, in vitro stability tests were performed in two media: phosphate buffered saline (PBS, pH=7.4) and freshly isolated mouse serum at 37°C. The radiopharmaceutical-containing samples were poured into microtubes and incubated. Samples were collected and analyzed at specific time intervals of 1, 2, 4, 6, 12, 24, and 48 hours. To determine the percentage of intact complex, ITLC with an appropriate mobile phase was used. After developing the ITLC strip, the distribution of radioactivity was measured using a gamma counter. The percentage stability was calculated as the ratio of the radioactive activity of the intact complex to the total activity at each time point. Each experiment was repeated three times.

Animal models and their treatment protocols

Female BALB/c nude mice (6-8 weeks old) were obtained from the Biochemistry and Biophysics Research Center, University of Tehran, Iran. Animals were maintained under specific pathogen-free conditions (22 ± 2 °C, 50 to 60% humidity, and a 12 h light/dark cycle) with free access to food and sterile water. All procedures were approved by the Institutional Animal Care and Use Committee of Tehran University of Medical Sciences (IR.TUMS.AEC.1403.115).

A total of 16 mice were randomly divided into four groups (n = 4 per group) according to the updated ARRIVE guidelines 2.0 [41]: Group A, tumor-bearing mice that were injected intravenously via the tail vein with ^{99m}Tc-DND-G2-Arg (100 µL, 30-40 MBq); Group B, a blocking group that received unlabeled L-arginine (0.5 mg/mL, 100 µL) immediately before administration of ^{99m}Tc-DND-G2-Arg injection; Group C, healthy control mice injected with $^{99m}TcO_4^-$; and Group D, tumor-bearing control mice injected with $^{99m}TcO_4^-$ (100 µL, 30–40 MBq). For tumor establishment, exponentially growing 4T1 cells were collected, washed with PBS, and subcutaneously inoculated into the right flank of mice in Groups A, B, and D (1×10^6 cells in 100 µL PBS). Tumor growth was monitored every 2 to 3 days using caliper measurements, and tumor volume was calculated using the formula (length × width²)/2. Imaging and biodistribution studies were performed when tumors reached 8 to 12 mm in diameter, approximately 3 weeks after inoculation.

In Vivo SPECT imaging and biodistribution

Mice were anesthetized with an intraperitoneal injection of ketamine/xylazine (100/10 mg/kg) and positioned in the prone position on the scanner bed. High-resolution SPECT imaging was carried out using a HiReSPECT II preclinical SPECT scanner (Persia Radiological Imaging Industries Development Company, Iran). Imaging was carried out with an energy window of 140 keV ± 20% for ^{99m}Tc. Semi-quantitative analysis was performed using maximum standardized uptake value (SUVmax) approximations based on region-of-interest (ROI) analysis with 3D Slicer software (display scale: 0 to 5, normalized to background activity).

Ex Vivo biodistribution studies

Immediately after the final imaging time point (2 h post-injection), mice were euthanized by ketamine overdose (200 mg/kg). Blood was harvested by cardiac puncture, and major organs such as heart, liver, spleen, lungs, kidneys, stomach, intestines, muscle, bone, and tumor were dissected, washed with normal saline, and then weighed. The radioactivity of each organ was determined by gamma counting (Delshid, Iran) with the appropriate energy window for ^{99m}Tc. Counts were corrected for background and physical decay. Results were expressed as percentage of injected dose per gram of tissue (%ID/g) using the following formula [42]:

$$\%ID/g = \left(\frac{\text{Radioactivity in tissue } (\mu Ci)}{\text{Tissue weight } (g) \times \text{Injected dose } (\mu Ci)}\right) \times 100$$

Kinetic modeling using a two-compartment model

A two-compartment kinetic model was used to quantitatively analyze the time-activity behavior of ^{99m}Tc-DND-G2-Arg in tumor tissue and major organs. The model includes two main components: (i) reversible exchange between blood and tissue compartments, and (ii) irreversible uptake in target tissue, primarily attributed to specific receptor binding or internalization processes. To implement the model, SPECT imaging data at 5, 30 and 120 minutes after injection were used, along with biodistribution data at 180 min. The activity measured in the heart region was used as a surrogate for plasma activity and served as the input function. For simplicity, the kinetics of the radiopharmaceutical in the tumor were described by a biexponential empirical model based on the following differential equation:

$$C_t(t) = \frac{K_1\, C_p(0)}{k_2 - k_3}\left(e^{-k_3 t} - e^{-k_2 t}\right)$$

The corresponding analytical solution was:

$$\frac{dCt}{dt} = K_1\, C_p(t) - (k_2 + k_3)C_t(t)$$

Where $C_p(t)$ represents the radiotracer concentration in target tissue at time t; $C_p(0)$ is the initial plasma concentration; K_1 stands for rate constant for transfer from blood to tissue (inflow); K_2 is the rate constant for reflux from tissue to blood (outflow); K_3 is the rate constant for irreversible trapping/binding in tissue (slow clearance from tumor). Tissue concentration values (C_t) were extracted from SPECT images using 3D Slicer software and normalized to %ID/g units using biodistribution data at 3 h. This hybrid approach enabled accurate temporal analysis of radiotracer behavior and comparison between different experimental groups.

Statistical analysis

Quantitative data are presented as the mean ± standard deviation (SD). Statistical analyses were performed using SPSS version 26 (IBM Corp., USA), GraphPad Prism version 9 (GraphPad Software, USA), and SigmaPlot version 14 (Systat Software, USA). Data normality was assessed using the Shapiro-Wilk test and Q-Q plots. Depending on data distribution, parametric tests (Student's t-test and one-way ANOVA followed by Tukey's post hoc test) or non-parametric tests (Mann-Whitney U test and Kruskal-Wallis test followed by Dunn's multiple-comparison test) were applied. A two-sided p value < 0.05 was considered statistically significant.

RESULTS

FTIR spectra characterization

For the G1 dendrimer, a distinct ester C-O stretching band was observed at 1279 cm^{-1}, confirming the successful formation of ester linkages between PEG and citric acid. The broad absorption band at 1154-1279 cm^{-1} was assigned to the alcoholic C-O stretching vibrations of PEG and citric acid, while the broad band at 3370-3500 cm^{-1} corresponded to the O-H stretching vibrations of the carboxylic acid groups derived from citric acid (Supplementary Material, Figure S1A).

For the G2 dendrimer, the appearance of an ester-related C-O band at 1232 cm^{-1} confirmed successful dendrimer growth through esterification between the terminal citric acid groups of the G1 dendrimer and the newly introduced citric acid units. A distinct peak at 1726 cm^{-1} was attributed to C=O stretching vibrations of the terminal citric acid groups. Additionally, the broad absorption between 2500 and 3430 cm^{-1} further confirmed the presence of carboxylic acid O-H groups (Supplementary Material, Figure S1B).

The FTIR spectra of the G2-PEG-citrate-ALGD-Arg is presented in Figure 1A. The strong band at 1650 cm^{-1} was attributed to amide C=O stretching vibrations, confirming the successful attachment of L-arginine to the dendrimer backbone. A weak band at approximately 1250 cm^{-1} further supported the presence of C-N stretching vibrations. The intense peak at 1100 cm^{-1} was characteristic of C-O-C ether stretching, confirming the presence of PEG chains on the dendrimer surface. The peaks at 1390 and 1440

cm^{-1} were assigned to the symmetric and asymmetric stretching vibrations of carboxylate groups, together with C-H bending vibrations, which are consistent with the citrate and PEG components of the conjugate. The strong band at 2935 cm^{-1} was attributed to the aliphatic C-H stretching vibrations of CH_2 and CH_3 groups.

Dynamic light scattering and zeta potential analysis

Based on DLS analysis, the initial measurements of the G1 dendrimers showed substantial aggregation, with an average particle size of approximately 326 nm (Supplementary Material, Figure S2A). Following dilution and 20 min of sonication, the particle size decreased to 75 nm (Supplementary Material, Figure S2B), indicating effective particle dispersion. The G1 dendrimers exhibited a zeta potential of -3.5 mV (Supplementary Material, Figure S2C).

Compared with G1, the G2 dendrimers displayed an improved size distribution with a mean hydrodynamic diameter of 91 nm and a single, sharp monodisperse peak (Supplementary Material, Figure S2D). They had a zeta potential of −3.3 mV (Supplementary Material, Figure S2E).

The physicochemical properties of the G2-PEG-citrate-ALGD-arginine conjugate were evaluated by DLS and zeta potential analysis (Figures 1B and 1C). The conjugate exhibited a Z-average hydrodynamic diameter of 202.4 nm, with a PDI of 0.376. Particle size distribution analysis revealed a bimodal profile, consisting of a smaller population at 6[illegible] nm (11%) and a dominant population at [illegible]1.6 nm (89%). A high-count rate of [illegible]29 kCPS indicated strong signal intensity and reliable measurement quality. Zeta potential analysis showed the presence of a negative surface charge of -7.3 mV, with a corresponding electrophoretic mobility of -5.7×10^{-5} $cm^2/V{\cdot}s$. All measurements were performed in a dispersion medium with a viscosity of 0.892 mPa·s and a conductivity of 6.606 mS/cm.

Surface and morphological analysis by FE-SEM

The FE-SEM images revealed spherical nanoparticles with uniform size distribution and smooth surface morphology (Figure 2A-2C). A limited degree of particle aggregation was observed, which may have resulted from sample preparation procedures or weak electrostatic interactions, consistent with the relatively low absolute zeta potential values. Particle size analysis based on 100 nanoparticles measured from multiple micrographs yielded an average diameter of 134.91 ± 15.01 nm (Figure 2D). The relatively small standard deviation (SD = 15.01 nm) indicates a well-controlled synthesis process with minimal size variability.

Findings from LC-MS analysis

The mass spectrum of G1 dendrimers exhibited characteristic fragmentation patterns with peaks at m/z 569 and m/z 652, corresponding to eight and nine PEG repeating units (CH_2-CH_2-O, M_W=44), respectively, conjugated to citric acid groups (Supplementary material, Figure S3A). Additional fragment ions separated by 44 Da further confirmed the PEG backbone of the dendrimer structure.

For the G2 dendrimers (Supplementary material, Figure S3B), the principal fragment ions were observed at m/z 606 (a citric acid unit linked to part of a second citric acid molecule and a partial PEG chain), m/z 512 (five PEG repeating units attached to citric acid), and m/z 696 (seven PEG repeating units associated with two complete citric acid groups). The characteristic bell-shaped fragmentation profile with regular 44-Da intervals confirmed successful dendrimer generation growth.

LC-MS analysis the G2-PEG-citrate-Arg conjugate identified several characteristic fragments confirming successful conjugation (Figure 3A). The major peak at m/z 573 confirmed successful conjugation of L-arginine, representing one L-arginine residue, one citric acid molecule, and two PEG repeating units (n = 2). The characteristic bell-shaped fragmentation pattern with 44-Da intervals was preserved, while the peak at m/z 705 corresponded to an L-arginine-conjugated structure containing one citric acid molecule and five PEG repeating units (n = 5).

In vitro cytotoxicity

Cell viability remained above 95% across all tested concentrations for both the G2 dendrimer and the G2-PEG-citrate-ALGD-arginine conjugate (Figure 3B). Notably, at concentrations exceeding 15.6 µg/mL, the L-arginine-conjugated dendrimers exhibited significantly higher cell viability than the unconjugated G2 dendrimers. Furthermore, enhanced cell proliferation was observed at higher concentrations of the G2-PEG-citrate-ALGD-arginine conjugate, which may be attributed to the role of L-arginine as a metabolic substrate and nutrient supporting cellular metabolism and proliferation.

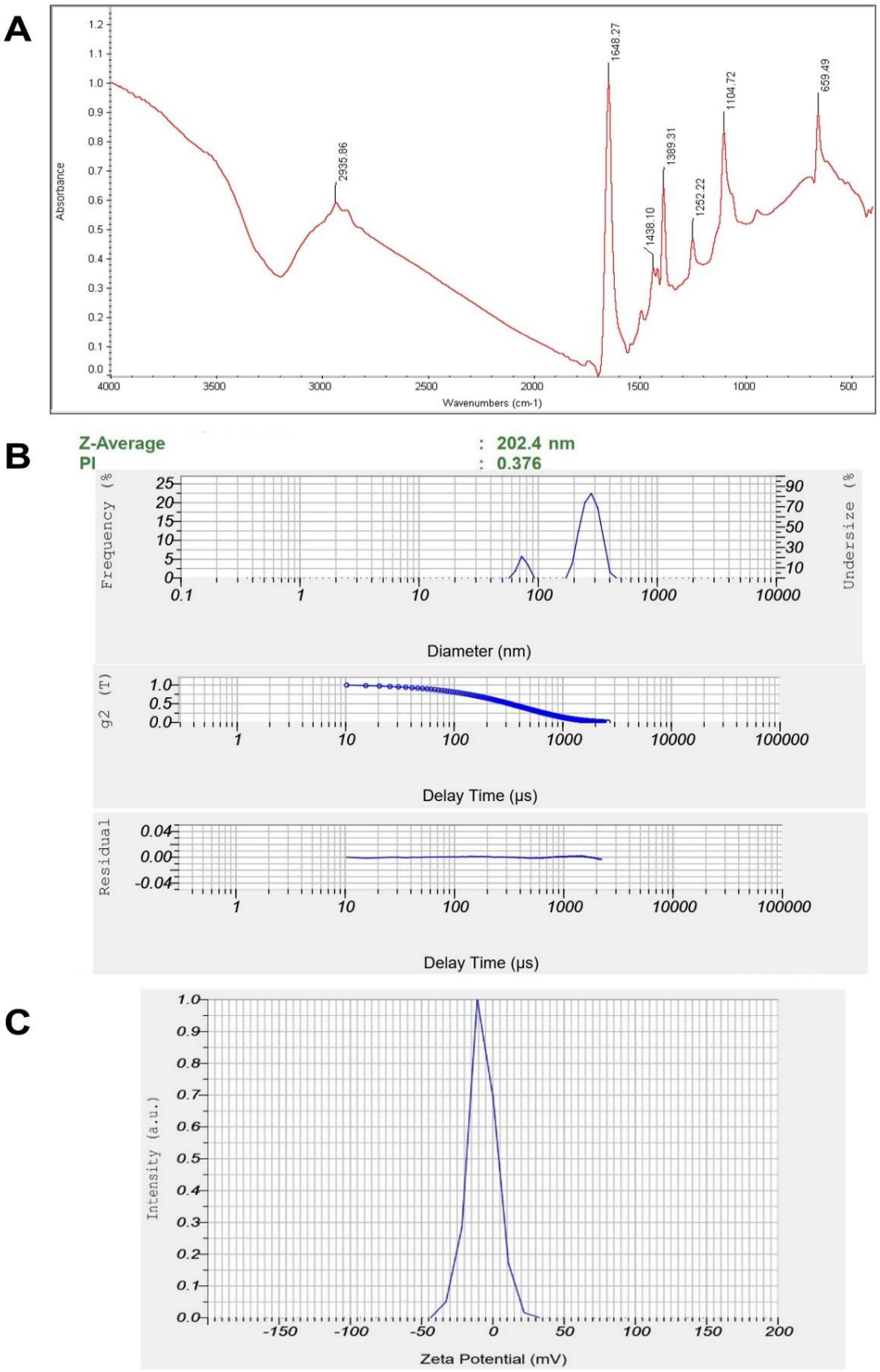

Fig. 1. Characterization of the G2-PEG-Citrate-Arg dendrimer conjugate. (A) FTIR spectrum confirming the successful conjugation of L-arginine to the dendrimer. (B) Size distribution histogram obtained from Dynamic Light Scattering (DLS). (C) Zeta potential distribution graph.

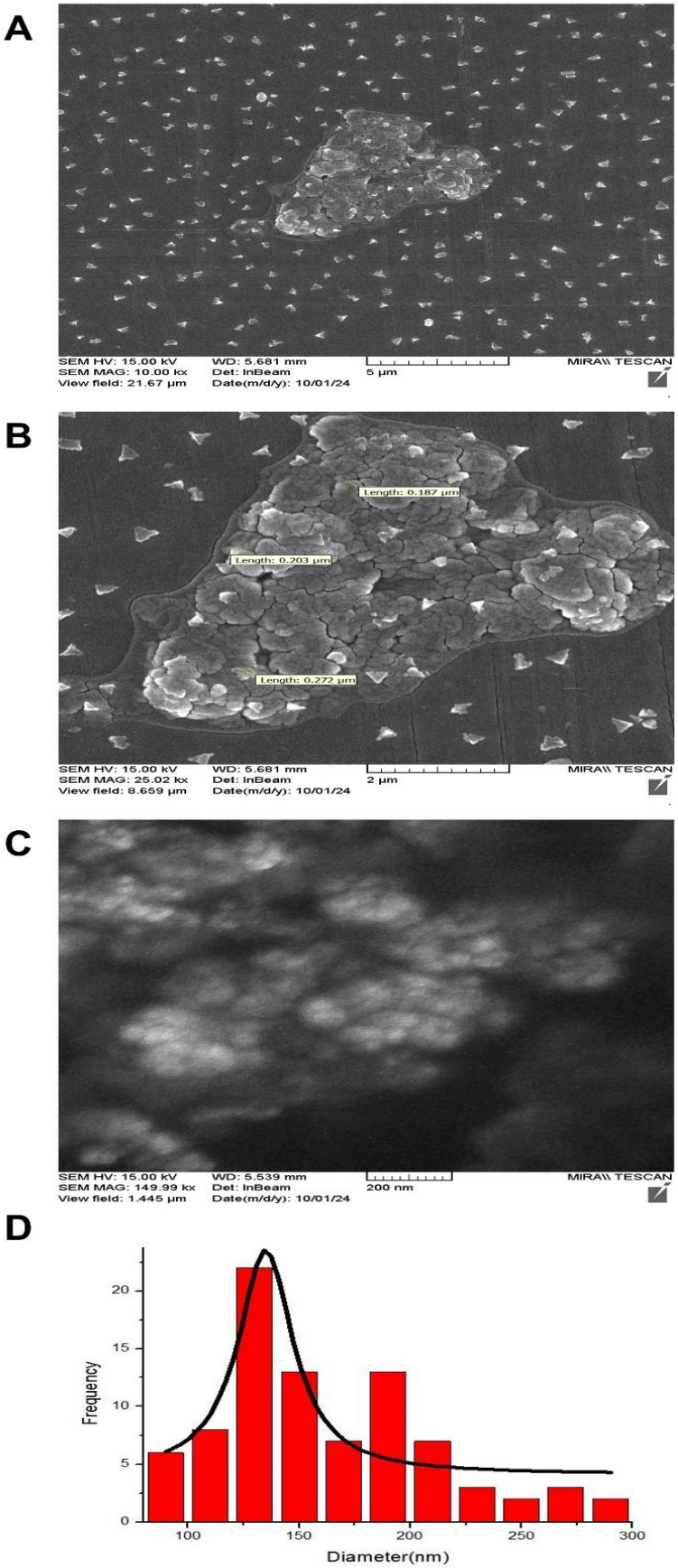

Fig. 2. FE-SEM characterization of the G2-PEG-Citrate-ALGD-Arginine Conjugates. Micrographs at different magnifications: (A) 5 µm, (B) 2 µm, and (C) 200 nm. (D) Particle size distribution histogram derived from FE-SEM images.

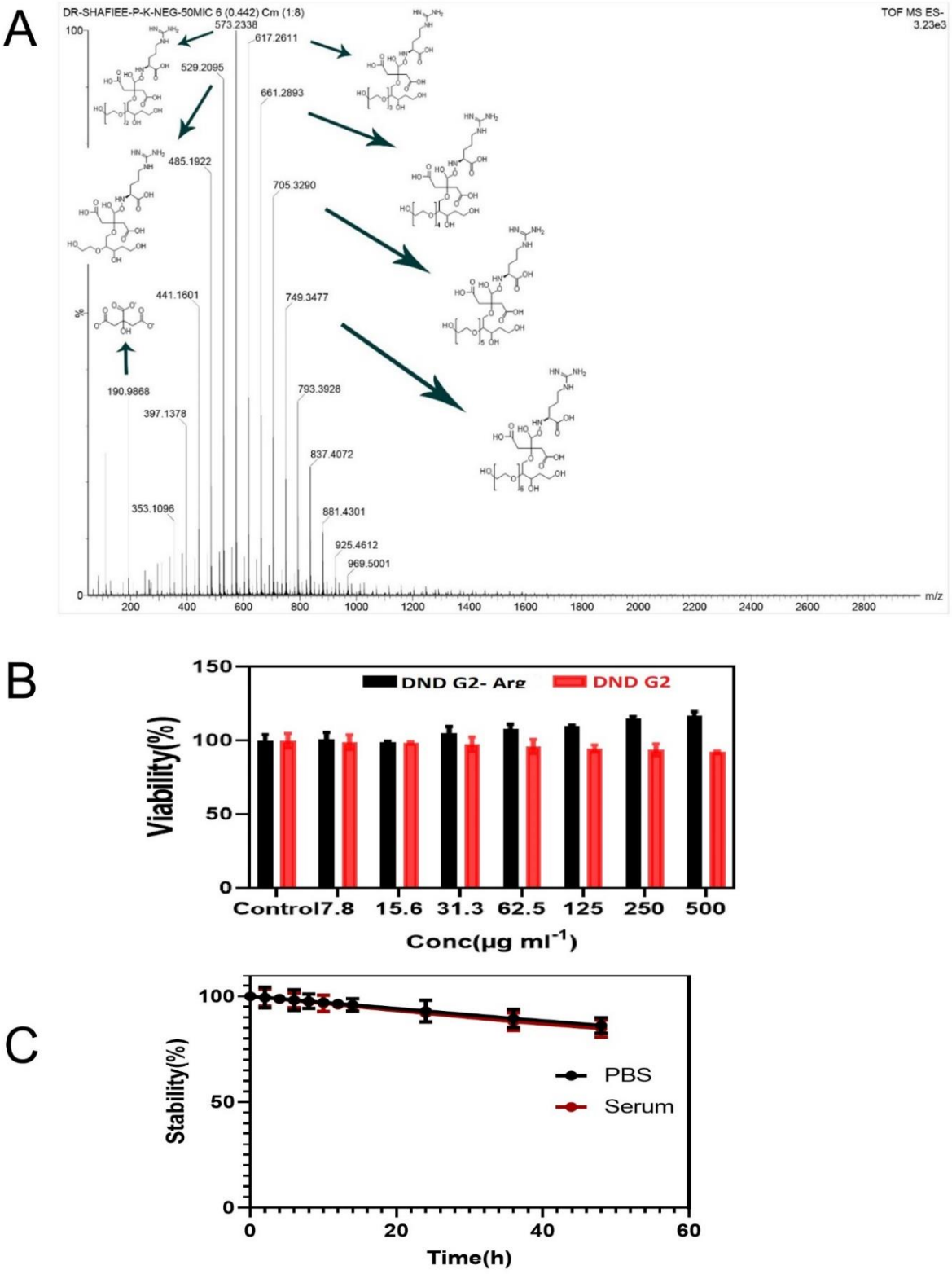

Fig. 3. (A) Liquid Chromatography-Mass Spectrometry (LC-MS) spectrum confirming the molecular weight and successful synthesis of the G2-PEG-Citrate-ALGD-Arg conjugate. (B) In vitro cytotoxicity of the G2 dendrimer and the G2-PEG-Citrate-ALGD-Arg conjugate against Vero cells, assessed by an MTT assay after 24 h of incubation. Cell viability is expressed as a percentage relative to untreated control cells. Data are presented as mean ± SD (n=3). (C) In vitro stability profile of the technetium-99m labeled conjugate (^{99m}Tc-Arg-DND G2) over 48 h. The complex was incubated in phosphate-buffered saline (PBS) and mouse serum at 37°C, and its radiochemical purity was determined at various time points by instant thin-layer chromatography (ITLC). Results are expressed as the mean percentage of intact complex ± SD (n=3).

Table 1. Radiolabeling efficiency and radiochemical purity of ^{99m}Tc-DND-G2-Arg evaluated by RTLC using different stationary and mobile phase systems.

Stationary Phase	Mobile Phase	Radiopharmaceutical Purity (%)	Free $^{99m}TcO_4^-$ (%)	Rf (Radiopharmaceutical)	Rf (Impurity; Free $^{99m}TcO_4^-$)
Silica TLC plate	Acetone	94.24	5.76	0.10	1.06
Whatman paper	Acetone	94.83	5.17	0.03	1.05
Silica gel	Acetone: Methanol (1:1)	94.51	5.49	0.04	1.05
Whatman paper	Acetone: Methanol (1:1)	94.63	5.37	−0.10	0.93
Silica gel	Methanol	99.68	0.32	−0.02	1.08
Whatman paper	Saline (0.9% NaCl)	87.01	12.99	0.04	0.77

Radiolabeling efficiency and stability

Radiochemical purity was evaluated by RTLC using various stationary and mobile phase systems to ensure comprehensive quality control (Table 1, Supplementary material, Figure S4). Among the tested systems, the silica gel/methanol combination provided the highest radiolabeling efficiency (99.68%; Figure 5S), with only 0.32% free pertechnetate, indicating excellent labeling yield. The radiolabeled conjugate remained at or near the origin (Rf = −0.02 to 0.10) in all chromatographic systems, confirming stable complex formation, whereas free pertechnetate migrated with the solvent front (Rf = 0.77–1.08). Under identical solvent conditions, Whatman paper exhibited slightly greater retention of the radiolabeled conjugate than silica gel, likely due to its higher hydrophilicity. No significant peaks corresponding to colloidal $^{99m}TcO_2$ (Rf = 0–0.1) were detected, indicating minimal formation of hydrolyzed or reduced technetium impurities. The negative Rf values observed in several systems further reflected strong retention of the radiolabeled conjugate on the stationary phase, supporting the robustness and stability of the radiolabeling process.

The stability of ^{99m}Tc-DND-G2-Arg was evaluated in PBS (pH 7.4) and fresh mouse serum at 37°C for 48 h (Figure 3C). The radiolabeled conjugate exhibited excellent stability, maintaining more than 95% radiochemical integrity during the first 6 h, corresponding approximately to one physical half-life of ^{99m}Tc, in both media. A gradual decline in radiochemical stability was observed thereafter, with 80–85% of the radiolabel remaining intact after 48 h. Although stability was slightly lower in mouse serum than in PBS, likely because of enzymatic degradation and metabolic interactions, the difference was not statistically significant ($p > 0.05$). These findings demonstrate that ^{99m}Tc-DND-G2-Arg possesses sufficient in vitro stability for potential in vivo SPECT imaging applications.

In Vivo biodistribution studies

Data are presented in Table 2. The biodistribution study for Group A showed that the mean uptake of the compound in tumor tissue was found to be 0.87 ± 0.19 %ID/g, ranging from 0.68 to 1.10 %ID/g. This shows that there was consistent uptake of the compound by the tumor tissue. The maximum uptake was found to be in the liver, i.e., 50.31 ± 6.03 %ID/g. Moderate uptake was found to be in the spleen and lungs, i.e., 5.11 ± 1.02 %ID/g and 4.76 ± 0.87 %ID/g, respectively. Low uptake was found to be in the heart, i.e., 0.46 ± 0.05 %ID/g. Absence of brain accumulation confirmed the inability to cross the blood-brain barrier. Regarding Tumor-to-background ratios, favorable ratios were observed for heart (1.866), intestines (1.50), and stomach (1.13), while liver and kidney ratios were modest (0.017 and 0.096, respectively).

To confirm that the uptake was receptor-mediated, a blocking experiment was conducted, where free L-arginine was administered to the tumor-bearing mice prior to the injection of the radiolabeled compound (Group B). The significant reduction of 31% in tumor uptake after L-arginine blockade was a strong indicator of active receptor-mediated uptake of the radiolabeled compound. The simultaneous increase in uptake in the liver and spleen was a reflection of the redistribution of the radiolabeled compound through the RES, as shown in the 22% and 30% increases, respectively, after tumor targeting was blocked. The significant reduction in renal uptake was an indicator of altered clearance kinetics, as shown in the 27% reduction p=0.002).

As a physiological control, healthy non-tumor-bearing mice received free ^{99m}Tc-pertechnetate (Group C). The classical biodistribution pattern of pertechnetate was observed with the predominant accumulation in the stomach (62.96 ± 7.53 %ID/g) via the sodium-iodide symporter (NIS) in gastric mucosa. Moderate uptake in the liver (10.37 ± 0.98 %ID/g) indicated partial hepatobiliary clearance, while low levels in the brain (0.20 ± 0.02 %ID/g) and heart (1.56 ± 0.16 %ID/g) confirmed rapid blood clearance and inability to cross the blood-brain barrier.

Table 2. Experimental Groups for In Vivo SPECT Imaging and Biodistribution Studies (n = 4 per group).

Treatment Group	Organ/Tissue	%ID/g (Mean ± SD)	CV (%)	Tumor-to-Background Ratios
Group A (Targeted Conjugates)	Tumor	0.87 ± 0.19	21.90%	-
	Liver	50.31 ± 6.03	11.98%	0.017 (Tumor/Liver)
	Kidneys	9.00 ± 1.03	11.48%	0.096 (Tumor/Kidney)
	Spleen	5.11 ± 1.02	21.12%	0.17 (Tumor/Spleen)
	Lungs	4.76 ± 0.87	18.17%	0.18 (Tumor/Lung)
	Heart	0.46 ± 0.05	11.71%	1.866 (Tumor/Heart)
	Brain	0.00	No uptake	∞ = N/A
	Intestines	0.58 ± 0.08	13.14%	1.50 (Tumor/Intestine)
	Stomach	0.77 ± 0.07	9.42%	1.13 (Tumor/Stomach)
	Carcass without the mentioned vital organs	1.38 ± 0.25	18.39%	0.63 (Tumor/Carcass)
Group B (Blocking Group)	Tumor	0.60 ± 0.24	39.40%	-
	Liver	61.58 ± 10.84	17.61%	0.010 (Tumor/Liver)
	Kidneys	6.38 ± 0.33	5.11%	0.094 (Tumor/Kidney)
	Spleen	6.62 ± 0.73	11.01%	0.090 (Tumor/Spleen)
	Lungs	6.68 ± 0.84	12.63%	0.089 (Tumor/Lung)
	Heart	0.89 ± 0.04	4.23%	0.669 (Tumor/Heart)
	Brain	0.00	NaN (no uptake)	∞ = N/A
	Intestines	0.60 ± 0.04	6.94%	0.996 (Tumor/Intestine)
	Stomach	2.50 ± 0.50	20.19%	0.239 (Tumor/Stomach)
	Carcass without the mentioned vital organs	1.55 ± 0.57	36.49%	0.385 (Tumor/Carcass)
Group C (^{99m}Technetium pertechnetate-treated healthy mice)	Tumor	-	-	-
	Liver	10.37 ± 0.98	9.46%	-
	Kidneys	3.38 ± 0.20	5.89%	-
	Spleen	3.92 ± 0.41	10.50%	-
	Lungs	4.37 ± 0.22	5.12%	-
	Heart	1.56 ± 0.16	10.19%	-
	Brain	0.20 ± 0.02	10.95%	-
	Intestines	3.51 ± 0.56	15.82%	-
	Stomach	62.96 ± 7.53	11.97%	-
	Carcass without the mentioned vital organs	3.24 ± 0.10	3.16%	-
Group D (^{99m}Technetium pertechnetate-treated tumor-bearing mice)	Tumor	0.42 ± 0.03	8.02%	—
	Liver	9.80 ± 0.80	8.14%	0.043 (Tumor/Liver)
	Kidneys	3.90 ± 0.22	5.63%	0.108 (Tumor/Kidney)
	Spleen	4.30 ±0.28	6.51%	0.098 (Tumor/Spleen)
	Lungs	4.60 ± 0.22	4.82%	0.091 (Tumor/Lung)
	Heart	1.42 ± 0.09	6.32%	0.296 (Tumor/Heart)
	Brain	0.20 ± 0.01	7.07%	2.100 (Tumor/Brain)
	Intestines	3.75 ± 0.25	6.57%	0.112 (Tumor/Intestine)
	Stomach	61.40 ± 4.36	7.10%	0.007 (Tumor/Stomach)
	Carcass without the mentioned vital organs	3.40 ± 0.12	3.60%	0.124 (Tumor/Carcass)

For the assessment of non-specific tumor accumulation, tumor-bearing mice were administered free ^{99m}Tc-pertechnetate (Group D). Pertechnetate exhibited minimal tumor uptake (0.42 ± 0.03 %ID/g), which was 2.1-fold lower than targeted Group A (0.87 %ID/g). Stomach dominance (61.40 ± 4.36 %ID/g) with 146-fold higher accumulation than tumor confirmed the unsuitability of pertechnetate for breast cancer imaging ($p<0.001$). The liver uptake (9.80 ± 0.80 %ID/g) was substantially lower than in dendrimer-treated groups (Groups A/B), indicating that the hepatic accumulation observed with ^{99m}Tc-DND-G2-Arg was due to nanoparticle characteristics rather than pertechnetate behavior.

Welch's ANOVA test confirmed the significant differences in liver accumulation among the groups ($F(3,7.8) = 92.6$, $p < 0.001$), with Groups A and B showing markedly higher liver uptake.

SPECT imaging studies

Semi-quantitative analysis of SPECT images showed evident differences in radiotracer biodistribution among the four experimental groups at different time points (Table 3 and Figure 4). Two-way repeated measures ANOVA revealed significant effects of group ($F(2,9) = 24.1$, $p < 0.001$),

time ($F(2,18) = 19.7$, $p < 0.001$), and interaction between group and time ($F(4,18) = 5.2$, $p = 0.006$) on tumor SUVs. Post-hoc Sidak tests showed that Group A had significantly higher tumor uptake than Group B at all time points ($p < 0.01$), and had better accumulation than Group D (pertechnetate control) at 30 minutes (4.8 ± 0.7 vs. 2.8 ± 0.4, $p = 0.008$). The maximum accumulation at 30 minutes in Group A was significantly different from both 5-minute and 120-minute time points ($p = 0.003$).

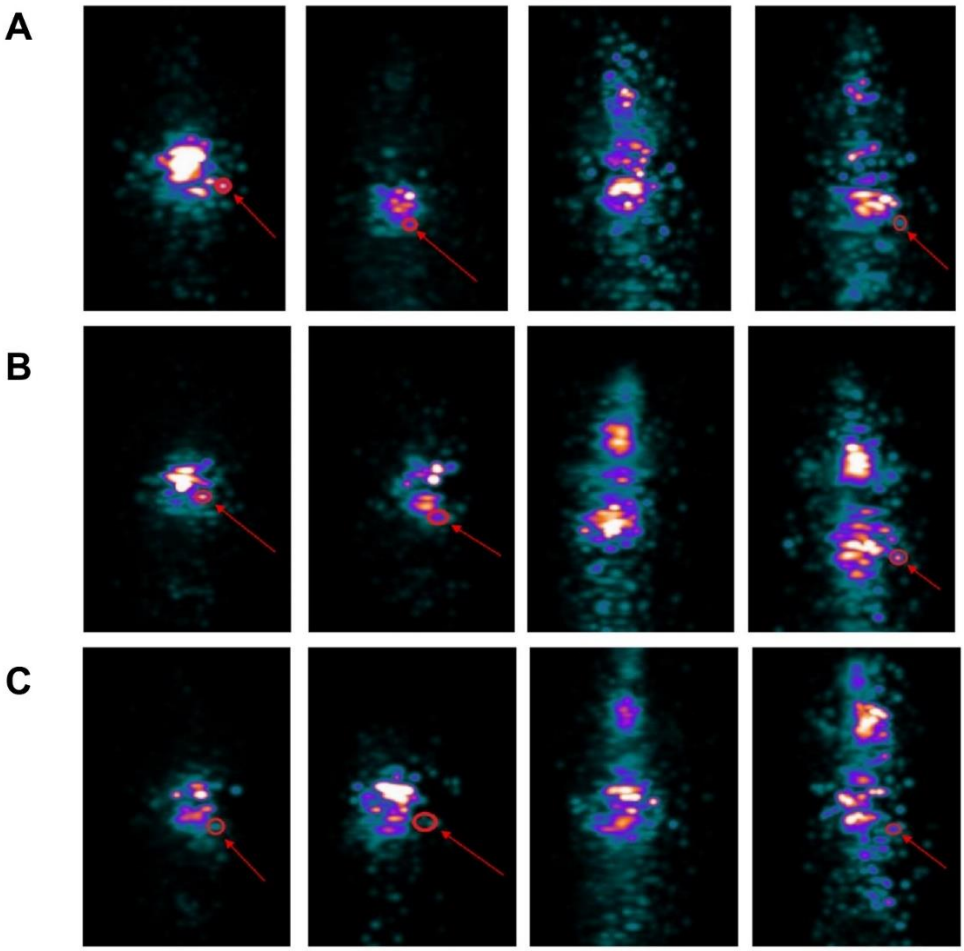

Fig. 4. Serial SPECT images of breast tumor-bearing BALB/c mice at (a) 5, (b) 30, and (c) 120 minutes following intravenous injection of radiotracers. Images are arranged from left to right for each time point: Group A (^{99m}Tc-DND G_2-Arg, targeted conjugate), Group B (^{99m}Tc-DND G_2-Arg following L-arginine blockade), Group C (^{99m}Tc-pertechnetate in healthy mice), and Group D (^{99m}Tc-pertechnetate in tumor-bearing mice). Arrows indicate tumor locations. Color scale represents relative radioactivity intensity (red > yellow > green > blue). Group A demonstrates clear tumor visualization at all time points with peak intensity at 30 minutes. Group B shows markedly reduced tumor uptake confirming receptor-mediated targeting. Groups C and D exhibit classic pertechnetate biodistribution with dominant stomach and thyroid accumulation, with Group D showing faint non-specific tumor uptake. These images collectively validate the targeting specificity of ^{99m}Tc-DND G_2-Arg and its superiority over free pertechnetate for breast cancer SPECT imaging.

Table 3. Semi-quantitative estimation of relative radiotracer uptake (SUVmax, scale 0-5) based on SPECT imaging at 5 minutes, 30 minutes, and 120 minutes after injection in the four experimental groups.

Treatment Group	Time (minutes)	Tumor	Blood (Heart)	Kidney	Stomach	Liver
Group A (Targeted Conjugate)	5	4.4	4.2	3.5	1.5	3.4
	30	4.8	2.05	4.0	2.1	4.3
	120	2.1	0.85	3.7	2.0	4.8
Group B (Blocking Group)	5	1.0	3.05	3.2	2.5	4.4
	30	1.4	1.90	4.3	3.0	4.85
	120	0.5	0.70	3.6	2.8	5.0
Group C (^{99m}Technetium pertechnetate-treated healthy mice)	5	---	3.55	1.2	5.0	3.25
	30	---	1.95	1.3	4.8	3.55
	120	---	0.5	1.0	4.7	4.05
Group D (^{99m}Technetium pertechnetate-treated tumor-bearing mice)	5	2.0	3.4	1.4	5.0	3.0
	30	2.8	1.7	1.5	4.9	3.3
	120	2.2	0.7	1.2	4.6	3.6

Pharmacokinetic and kinetic modeling analysis

Two-compartment kinetic modeling was used to analyze the in vivo distribution of the radioligand in tumor tissue and blood (heart) in all experimental groups (A-D). Time-activity curves (TACs) were derived from dynamic SPECT/CT images obtained at 5, 30, and 120 min post-injection and normalized to ex vivo biodistribution measurements at 180 min. This allowed for semi-quantitative analysis of the principal kinetic parameters controlling radioligand transport, retention, and clearance (Figure 5).

In Group A, the tumor uptake showed a steep increase after injection, reached a definite peak around 30 min, and then gradually decreased, remaining detectable up to 180 min. In contrast, blood radioactivity showed a sharp decline with time. Kinetic analysis showed a high influx rate constant (K_1 = 0.243 min^{-1}), a large irreversible trapping rate constant (k_3 = 0.119 min^{-1}), and a low rate of efflux (k_2 = 0.032 min^{-1}). The fact that the value of k_3 was much larger than that of k_2 ($k_3 \gg k_2$) indicated a strong and specific receptor-mediated uptake, resulting in a prolonged retention in the tumor and an increasingly higher tumor/blood ratio with time.

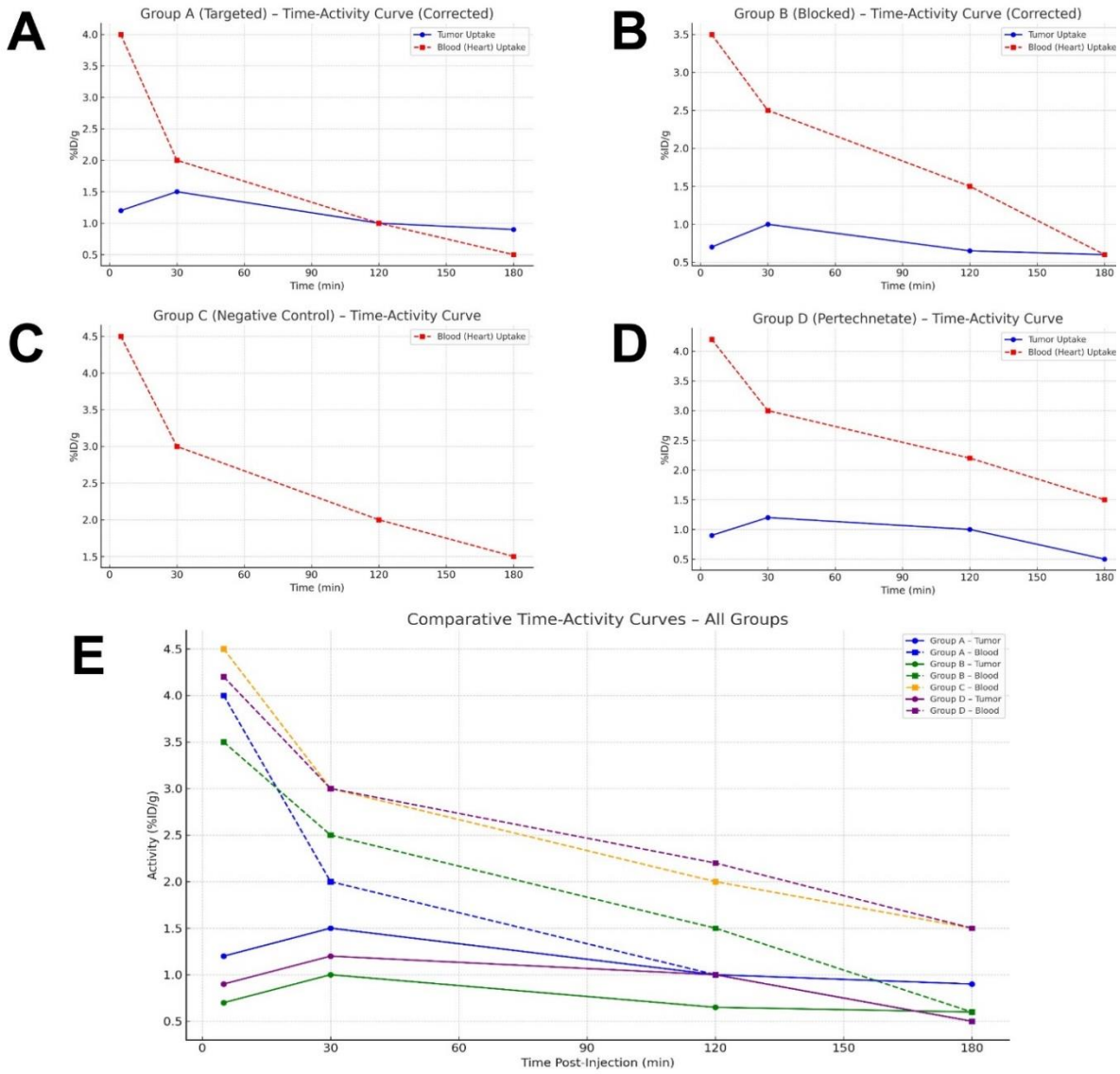

Fig. 5. Pharmacokinetic profiles of radiotracers in tumor and blood. (A-D) Time-activity curves extracted from SPECT/CT imaging (5, 30, 120 min) and normalized to *ex vivo* biodistribution data (180 min) for (A) Group A (targeted, 99m99mTc-DND-G_2-Arg), (B) Group B (blocking), (C) Group C (negative control, non-tumor bearing), and (D) Group D (non-specific, 99m99mTc-pertechnetate). (E) Complex time-activity curves comparing all four experimental groups. Solid and dashed lines represent uptake in the tumor and blood (heart), respectively. Group A demonstrates specific tumor uptake with rapid blood clearance. In contrast, the lower and more transient uptake in Groups B and D confirms the specificity of the targeted probe, while Group C shows only background blood-pool activity.

In Group B, there was a significant reduction in uptake at all-time points due to the competitive blockade of the receptor, with a reduction of about 57% in early tumor activity compared with Group A ($p < 0.01$). This was accompanied by significant changes in the kinetic parameters, where there was a reduction in the influx rate (K_1 = 0.151 min^{-1}), a significant reduction in the trapping constant (k_3 = 0.021 min^{-1}), and an increase in the efflux rate (k_2 = 0.045 min^{-1}). This finding confirmed that the increased uptake in tumors of Group A was receptor-specific.

The kinetic data for Group C could be fitted satisfactorily using a single-compartment blood pool model, indicating a progressive decrease in systemic activity with time and no sign of tissue retention. This finding reflected the background pharmacokinetics in the absence of tumor tissue. In Group D, there was moderate initial tumor uptake. However, this was followed by rapid washout. Although the rate of influx was moderate (K_1 = 0.202 min^{-1}), the trapping constant was very low (k_3 = 0.008 min^{-1}), ruling out the possibility of specific binding and further confirming the non-specific accumulation pattern.

DISCUSSION

In the present investigation, we designed and characterized a technetium-99m–labeled anionic linear-globular PEG citrate dendrimer conjugated with L-arginine as a potential imaging agent for breast cancer detection using SPECT imaging in a preclinical model. The design rationale combined physicochemical optimization for passive tumor accumulation with biological functionalization to enable active targeting, with encouraging results in terms of radiochemical purity, in vitro stability, and in vivo imaging characteristics.

The hydrodynamic diameter of the nanoparticles (202.4 nm) falls within the optimal range (100–300 nm) for enhanced permeability and retention (EPR) effect-mediated tumor targeting, allowing extravasation through fenestrated tumor vasculature [43, 44]. The moderate polydispersity (PDI = 0.376) is acceptable for dendritic nanoparticles and comparable to other ALGD systems [40, 45, 46]. FE-SEM analysis confirmed spherical morphology with an average diameter of 134.91 ± 15.01 nm. The expected discrepancy between hydrodynamic diameter and FE-SEM measurements reflects the hydrated PEG corona and solvent layer surrounding the nanoparticles in aqueous environments, a well-documented phenomenon for PEGylated systems [44, 47-50]. The moderately negative zeta potential (−7.3 mV) suggests weak electrostatic repulsion; however, PEGylation provides steric stabilization as the primary mechanism for maintaining colloidal stability, consistent with previous reports [31, 40, 49].

FTIR and LC-MS analyses confirmed successful L-arginine conjugation to the G2 dendrimer backbone. The appearance of amide C=O stretching (1650 cm^{-1}) and characteristic fragmentation patterns in LC-MS (m/z 573, 705) verified the presence of arginine moieties while retaining the PEG-based structure (44-Da intervals). The MTT assay demonstrated excellent cytocompatibility (>95% viability at all concentrations tested), with enhanced viability observed at concentrations above 15.6 µg/mL for the arginine-conjugated dendrimer. This proliferative effect likely reflects arginine utilization in cellular metabolism, consistent with its role in polyamine biosynthesis and nitric oxide production via nitric oxide synthase [51-53]. The observed proliferative activity could be related to the utilization of arginine by HeLa cells, which have been shown to express enzymes responsible for arginine metabolism [54, 55].

The G2-PEG-Citrate-ALGD-Arg conjugate achieved high radiolabeling efficiency (>99%) across various chromatographic systems, with the silica/methanol system performing optimally (99.68% efficiency, 0.32% impurity; Figure 5S). The superior performance of this system likely results from polar interactions between silica hydroxyl groups and the PEGylated dendrimer surface, favoring retention of the labeled conjugate at the origin, while free pertechnetate migrates with the solvent front [56, 57]. Moreover, literature on the QC of radiopharmaceuticals has shown that mobile phases containing methanol are effective for the separation of radiolabeled compounds from free radionuclide impurities [58-60]. A specific study on the QC of ^{68}Ga-DOTATATE was conducted, where the mobile phase containing methanol and ITLC-SG was used, and the results showed that an increase in the proportion of methanol in the mobile phase could reduce the development time, yet maintain resolution and peak shape [60]. This confirms that methanol provides optimal solvation and migration of free radionuclide species without disrupting the integrity of the labeled conjugate.

The four-group experimental design (targeted conjugate, blocking, and pertechnetate controls) conclusively demonstrated active targeting. Group A showed tumor uptake of 0.87 ± 0.19 %ID/g, which was significantly reduced to 0.60 ± 0.22 %ID/g (31% reduction, $p = 0.03$) upon L-arginine blockade, confirming receptor-mediated uptake. The targeting mechanism likely involves overexpression

of cationic amino acid transporters (particularly CAT-1) on breast cancer cells, as well as arginine-utilizing enzymes such as inducible nitric oxide synthase (iNOS) in the tumor microenvironment [34, 35, 61, 62]. In fact, macrophages and endothelial cells in the tumor microenvironment may express high levels of iNOS enzymes, which require L-arginine as a substrate to produce nitric oxide [63]. This strategy aligns with previous studies demonstrating amino acid-functionalized dendrimers for tumor-specific imaging, including ^{99m}Tc-labeled dendrimer-phenylalanine conjugates targeting LAT1 transporters for brain tumor imaging [39] and Gd^{3+}-labeled dendrimer-asparagine conjugates for colon cancer imaging [64].

One of the key questions in nanomedicine research is the relative contribution of passive targeting (via the EPR effect) versus active receptor-mediated targeting to overall tumor accumulation [65]. In the present study, we aimed to obtain an approximate estimate of this partitioning by including a blocking group (Group B), in which animals received an excess of free arginine before administration of the radiolabeled conjugate, to competitively inhibit specific ligand-receptor interactions. The mean tumor uptake in the targeted group (Group A) was 0.87 %ID/g, whereas that in the blocking group (Group B) was 0.60 %ID/g. Assuming that the residual uptake observed in the blocking group largely reflects non-specific mechanisms, primarily the EPR effect and other passive accumulation processes, we estimated that approximately 69% of the total tumor uptake is attributable to EPR-mediated passive targeting, while the remaining 31% is attributable to active targeting resulting from specific ligand–receptor binding. This estimation is consistent with the widely accepted view that, in many preclinical tumor models, the EPR effect plays a dominant role in nanocarrier extravasation and retention, while active targeting enhances cellular internalization and prolonged retention within the tumor microenvironment [65]. Notably, the observed 31% contribution from active targeting is non-negligible and likely reflects successful conjugation of arginine to the PEGylated dendrimer, enabling improved interaction with tumor-associated transporters or receptors. However, it is important to interpret these values with caution. The calculated fractions are approximate estimates rather than precise quantitative determinations, and several factors may influence this partitioning. First, the blocking efficiency may not be complete, as residual receptor availability or incomplete competitive inhibition could lead to underestimation of the active targeting component. Second, the EPR effect itself is highly heterogeneous, depending on tumor type, size, vascular permeability, and stromal architecture [65, 66]. Third, the use of a dedicated non-targeted nanocarrier (identical formulation without arginine) would provide a more direct and accurate control for passive uptake, which was beyond the scope of the current study.

To put the preliminary performance of our ^{99m}Tc-labeled nanoconstruct into context, it is informative to compare its imaging properties with those of established SPECT radiopharmaceuticals for breast cancer imaging, such as ^{99m}Tc-sestamibi (MIBI), which remains a widely used agent in clinical practice. MIBI has a rapid uptake in tumors because of high first-pass extraction, allowing imaging as early as 5-10 minutes following injection [67]. Nonetheless, MIBI has been shown to have substantial washout over time, with rates of clearance dependent on tumor blood flow and P-glycoprotein (P-gp) expression. The reported washout half-times for MIBI in breast tumors have varied from 98 to 696 minutes, with quicker washout rates in tumors with higher blood flow [68]. This washout phenomenon requires careful timing of imaging, usually done using early (10-30 min) and delayed (60-120 min) imaging protocols to evaluate both perfusion and retention properties [69]. Our nanoconstruct showed a different kinetic profile, with peak tumor uptake at 30 minutes (SUV 4.8), followed by a gradual decrease to an SUV of 2.1 at 120 minutes. This kinetic profile, with $k_3 >> k_2$ in compartmental analysis, suggests binding-related retention, which may offer certain advantages over MIBI's perfusion-related retention, though direct comparative studies would be needed to confirm this. Although MIBI's uptake is known to be highly correlated with tumor blood flow (r values not specified but significant positive correlation found) [68], our nanoconstruct's active targeting strategy ensures specificity irrespective of perfusion differences, which could be a major advantage in tumor imaging with heterogeneous vascularity.

The lesion-to-background (L/B) ratio is an important factor for image quality and interpretability. In a comparative study of MIBI and ^{99m}Tc-maraciclatide (an αvβ3 integrin-targeted angiogenesis agent) with high-resolution dedicated gamma cameras, mean L/B ratios of 1.55 ± 0.36 for MIBI and 1.62 ± 0.37 for maraciclatide were found in malignant breast lesions (p = 0.53) [70]. Our nanoconstruct yielded tumor-to-muscle ratios of 0.63 (Group A at about 2.5 h), which, although lower than the L/B ratios, must be evaluated in the context of the differences in measurement approach (tumor-to-muscle vs. lesion-to-

background within the breast) and imaging instrumentation. Notably, our tumor-to-stomach ratio of 0.44 reflects a 63-fold improvement over pertechnetate controls, remedying an important shortcoming of existing agents that concentrate heavily in gastric mucosa, potentially obscuring thoracic or abdominal imaging.

The predominant hepatic accumulation observed for ^{99m}Tc-DND-G2-Arg is consistent with the well-recognized biodistribution profile of PEGylated dendrimer-based nanocarriers. For instance, Okuda et al. demonstrated that intravenously administered PEGylated dendritic poly(L-lysine) preferentially accumulated in the liver and kidneys in a generation-dependent manner, supporting the notion that hepatic sequestration is an inherent characteristic of dendrimer-based systems rather than a unique feature of the present formulation [71]. Likewise, Medina et al. reported that PEGylation substantially reduced, but did not eliminate, liver accumulation of G5 PAMAM dendrimers. This highlights the important role of surface engineering in modulating mononuclear phagocyte system (MPS) uptake [72]. The increased liver accumulation observed following L-arginine blockade further supports this mechanism. When receptor-mediated tumor targeting was inhibited, the radiotracer was redistributed toward the liver and spleen, consistent with competitive disposition kinetics in which nanoparticles that fail to localize to their intended target are preferentially cleared by the reticuloendothelial system [73]. Although this biodistribution pattern is mechanistically consistent with previous reports, the pronounced hepatic uptake represents the principal obstacle to clinical translation of the present nanoradiotracer. Importantly, liver accumulation was approximately five-fold higher than that observed with free ^{99m}Tc-pertechnetate, confirming that this behavior is attributable to the nanoparticle platform rather than nonspecific technetium distribution. While high hepatic background is unlikely to interfere with visualization of primary breast tumors, it may substantially reduce lesion-to-background contrast for hepatic metastases and thereby compromise accurate disease staging. In addition, prolonged liver retention may increase radiation exposure to normal hepatic tissue, an important consideration for dosimetry, particularly if repeated imaging studies are required. Consequently, reducing hepatic sequestration should be considered a priority for further optimization before clinical translation. Several rational design strategies may improve the biodistribution profile of this platform. Increasing PEG density or molecular weight may provide greater steric shielding and reduce MPS recognition [32], while zwitterionic surface modifications have shown promise in minimizing nonspecific protein adsorption and macrophage uptake [73]. Further optimization of nanoparticle size within the lower enhanced permeability and retention range may also alter protein corona formation and improve systemic distribution [43, 44]. In addition, alternative dendritic architectures with enhanced stealth characteristics may further reduce hepatic clearance and prolong circulation time [26].

Renal uptake was moderate in Group A at 8.75 ± 1.07 %ID/g, with a 27% reduction after blocking ($p = 0.002$). This is in accordance with the Okuda study that showed that PEGylated KG6 accumulated in the liver and kidney, with renal distribution being PEGylation-dependent [71]. Of interest is that our renal accumulation of 202 nm nanoparticles refutes the conventional view that glomerular filtration is limited to nanoparticles of diameter <6 nm [74]. Naumenko et al. used intravital microscopy to show that PEGylated 140 nm nanoparticles accumulated transiently in the kidney with rapid translocation of the nanoparticles from the peritubular capillaries to the tubular epithelial cells and subsequent excretion into the lumen of the kidney within 60 min post-injection [75]. The presence of intact full-sized nanoparticles was confirmed using transmission electron microscopy to be present in the urine 2 hours post-injection, showing an alternative mechanism of renal clearance of nanoparticles >6 nm diameter [75]. This gives credence to our renal accumulation results, with the moderate renal uptake of Group A potentially being useful for the clearance of the nanoparticles.

The additional 30% increase in spleen uptake with blocking (Group B vs. A, $p=0.02$) also supports the concept of redirected MPS uptake when specific tumor pathways are saturated. Early studies by Peracchia et al. on PEGylated polycyanoacrylate nanoparticles showed that PEGylation led to a significant decrease in hepatic uptake with a concomitant marked increase in spleen uptake, indicating that surface modification can redirect nanoparticles to splenic filtration pathways [76]. The finding that blocking tumor targeting resulted in an increase in splenic uptake also supports the redirected clearance concept and confirms that the nanoconstruct interacts with biological recognition systems that are susceptible to competitive inhibition.

The low stomach uptake in Groups A and B (0.77% and 2.50% ID/g) relative to the massive uptake in pertechnetate controls (61-63% ID/g) offers conclusive proof of radiolabel stability. The 60-80 fold difference is especially important in light of the established pharmacokinetics of free pertechnetate. Pertechnetate ions concentrate transiently in salivary glands, choroid plexus, stomach (gastric mucosa), and thyroid gland because of an ionic pump mechanism common to iodide [77]. After intravenous injection, pertechnetate is eliminated by three processes: rapid diffusion into interstitial fluid, intermediate-rate concentration in glandular tissues, and slow glomerular filtration [78].

Limitations and translational considerations

Some limitations need to be overcome for clinical translation. The major limitation is that of liver uptake, which presents two challenges for clinical translation. Firstly, while primary breast tumors may not be obscured by hepatic uptake, any metastasis to this organ may be obscured by the high background, which may compromise staging. Secondly, the dose to the liver from multiple imaging studies must be evaluated to comply with safety regulations. The 5-6 fold higher uptake of these particles relative to pertechnetate controls clearly indicates that this uptake is mediated by the nanoparticles rather than non-specific technetium uptake.

Although tumor visualization is possible, the tumor-to-background ratios are moderate, which may affect the detection of small metastases or micro-tumors smaller than 2 mm. Improvement of tumor retention through: (i) multivalent presentation of L-arginine to enhance avidity [79]; (ii) inclusion of higher-affinity targeting ligands such as RGD peptides or folate in conjunction with L-arginine [80]; or (iii) application of stimuli-based mechanisms such as pH-dependent release or enzymatically cleavable linkers may enhance tumor targeting [81].

To be considered for clinical translation, the nanoconstruct would need to demonstrate comparable or improved diagnostic performance relative to existing imaging methods for breast cancer, which would require prospective comparative studies. The existing standard of care for imaging is ^{18}F-FDG PET/CT for staging and restaging, and ^{99m}Tc-sestamibi for specific indications [82, 83]. The following comparisons should be made between the nanoconstruct and the existing methods: (i) diagnostic accuracy (sensitivity and specificity) compared to histopathology; (ii) ability to image small lesions (<1 cm) and axillary nodal involvement; (iii) performance in specific clinical applications (such as assessment of response to therapy and detection of recurrence); and (iv) practical considerations such as same-day imaging, low interference from physiological uptake, and good safety profile.

Finally, another limitation of the present study is the lack of quantitative determination of the degree of arginine substitution on the PEGylated dendrimer. While successful conjugation was confirmed by FTIR, LC-MS, and physicochemical analyses, exact ligand density was not measured due to budget constraints. Consequently, the precise relationship between arginine loading and targeting efficiency could not be established. Future studies should include quantitative characterization of ligand conjugation to enable more systematic optimization of the nanocarrier design. Despite this limitation, the functional evidence from biodistribution and blocking studies supports the successful formation and receptor-mediated targeting capability of the developed nanoplatform.

Collectively, the imaging performance observed in this study should be considered preliminary and specific to the xenograft model employed; further evaluation in orthotopic models, larger animal cohorts, and comparison with established clinical SPECT tracers will be necessary to validate these findings.

CONCLUSION

Overall, ^{99m}Tc-DND-G2-Arg shows promise as a proof-of-concept targeted nanoradiotracer for SPECT imaging of breast cancer in preclinical models. The combination of PEGylated anionic linear-globular dendrimers with L-arginine-mediated targeting resulted in encouraging properties, including favorable radiochemical stability, good biocompatibility, specific tumor uptake, rapid blood clearance, and promising in vivo pharmacokinetics in this initial evaluation. The concordance of biodistribution, blocking studies, SPECT imaging, and kinetic analysis further supports the specificity and imaging potential of this platform.

Although further optimization is needed to reduce hepatic uptake, improve tumor-to-background contrast, and validate its performance in comprehensive translational studies, these findings establish ^{99m}Tc-DND-G2-Arg as a strong candidate for continued preclinical development. The modular dendrimer architecture may provide a versatile platform for future incorporation of alternative targeting ligands or therapeutic

payloads, suggesting potential for further development in targeted SPECT imaging and theranostic applications, though additional optimization and validation studies are warranted.

ACKNOWLEDGEMENTS

None.

CONFLICTS OF INTEREST

The authors declare no competing interests.

FUNDING

None.

ETHICAL CONSIDERATIONS

Ethics approval was received from the Institutional Animal Care and Use Committee of Tehran University of Medical Sciences (IR.TUMS.AEC.1403.115).

AUTHORS' CONTRIBUTIONS

P K: Investigation, methodology, writing–original draft. **M Sh A:** Project administration, conceptualization, supervision, Investigation, methodology, writing – review and editing. **M A:** Investigation, methodology, writing–original draft. **T Z M:** Project administration, conceptualization, supervision, Investigation, methodology, writing – review and editing. **M M:** Investigation, methodology, writing–original draft. **H E Sh:** Data Curation, Software, writing–original draft. **A J:** Investigation, methodology. **S M A:** Writing – original draft.

DECLARATION OF ARTIFICIAL INTELLIGENCE (AI)

During the preparation of this review, the authors utilized ChatGPT for grammar checking, refining readability, and preparing the graphical abstract. The content was not generated by AI; it was only used as a tool for enhancement. After applying these tools, the authors carefully reviewed and edited the content as necessary and take full responsibility for the material presented in this publication.

DATA AVAILABILITY

Not applicable.

REFERENCES

1. Elhawary NA, Ekram SN, Sembawa HA, Tashkandi E, Bannani S, Azher ZA, et al. Descriptive epidemiology of female breast cancer around the world: incidence, mortality, and sociodemographic risks and disparities. Int J Environ Health Res. 2025;35(12):3648-3662.
2. Organization tWH: Breast cancer. https://www.who.int/news-room/fact-sheets/detail/breast-cancer 2025. Accessed.
3. Bray F, Laversanne M, Sung H, Ferlay J, Siegel RL, Soerjomataram I, et al. Global cancer statistics 2022: GLOBOCAN estimates of incidence and mortality worldwide for 36 cancers in 185 countries. CA Cancer J Clin. 2024;74(3):229-263.
4. Khan AQ, Touseeq M, Rehman S, Tahir M, Ashfaq M, Jaffar E, et al. Advances in breast cancer diagnosis: a comprehensive review of imaging, biosensors, and emerging wearable technologies. Front Oncol. 2025;15:1587517.
5. Comparetto C, Borruto F. Cutting-edge imaging breakthroughs for early breast cancer detection. Cancer Screen Prev. 2025;4(1):21-39.
6. Bodewes FTH, Van Asselt AA, Dorrius MD, Greuter MJW, De Bock GH. Mammographic breast density and the risk of breast cancer: a systematic review and meta-analysis. The Breast. 2022;66:62-68.
7. Sidiropoulou Z, Fonseca V. A systematic review of the cost-effectiveness of screening modalities for breast cancer in european countries. Cancers. 2025;17(21):3585.
8. Aktokli N, Polycarpou I, Themistocleous SC, Sophocleous D, Mamais I. comparison of the diagnostic performance of magnetic resonance imaging (MRI), ultrasound and mammography for detection of breast cancer based on tumor type, breast density and patient's history: a review. Radiography. 2022;28(3):848-856.
9. Abeelh EA, AbuAbeileh Z. Comparative effectiveness of mammography, ultrasound, and MRI in the detection of breast carcinoma in dense breast tissue: a systematic review. Cureus. 2024;16(4):e59054.
10. Katal S, McKay MJ, Taubman K. PET molecular imaging in breast cancer: current applications and future perspectives. J Clin Med. 2024;13(12):3459.
11. Schnitzer ML, Kremer C, Hertel A, Haselmann V, von Münchhausen N, Schoenberg SO, et al. Economic assessment of molecular imaging in the oncology treatment process. Eur J Radiol. 2022;146:110105.
12. Karssemakers LHE, Besseling LMP, Schoonmade LJ, Su N, Nolte JW, Raijmakers PG, et al. Diagnostic accuracy of bone SPECT and SPECT/CT imaging in the diagnosis of unilateral condylar hyperplasia: A systematic review and meta-analysis. J Craniomaxillofac Trauma. 2024;52(4):447-453.
13. Mushtaq S, Bibi A, Park JE, Jeon J. Recent progress in technetium-99m-labeled nanoparticles for molecular imaging and cancer therapy. Nanomaterials. 2021;11(11):3022.
14. Kane SM, Padda IS, Patel P, Davis DD. Technetium-99m. StatPearls [Internet]. StatPearls Publishing; 2024.
15. Jiao D, Chen X, Sun X, Lu Z, Dai H, Wang C, et al. A comparative study of mitoxantrone hydrochloride injection and technetium-99 m for tracing axillary sentinel nodes in patients with breast cancer. BMC cancer. 2025;25(1):209.
16. Maddineni S, Tosoni SM, Sunwoo JB, Baik FM. Comparison of technetium-99m tilmanocept to

technetium-99 sulfur colloid radiotracer for sentinel lymph node biopsy in head and neck melanoma. Ann Otol Rhinol Laryngol. 2025;134(7):485-492.
17. Trusova V, Karnaukhov I, Zelinsky A, Borts B, Ushakov I, Sidenko L, et al. Technetium-99m: a nanomaterial perspective. Ukr J Phys. 2024;69(9):642-.
18. Mehrizi TZ, Ardestani MS, Molla Hoseini MH, Khamesipour A, Mosaffa N, Ramezani A. Novel nano-sized chitosan amphotericin b formulation with considerable improvement against leishmania major. Nanomedicine (Lond). 2018;13(24):3129-3147.
19. Bober Z, Bartusik-Aebisher D, Aebisher D. Application of dendrimers in anticancer diagnostics and therapy. Molecules. 2022;27(10):3237.
20. Cruz A, Barbosa J, Antunes P, Bonifácio VDB, Pinto SN. A glimpse into dendrimers integration in cancer imaging and theranostics. Int J Mol Sci. 2023;24(6):5430.
21. Gonciarz A, Pich R, Bogdanowicz KA, Pellowski W, Miedziak J, Lalik S, et al. Review of current achievements in dendrimers and nanomaterials for potential detection and remediation of chemical, biological, radiological and nuclear contamination—integration with artificial intelligence and remote sensing technologies. Nanomaterials. 2025;15(18):1395.
22. Ebrahimi S, Sadeghizadeh M, Aghasadeghi M, Shafiee Ardestani M, Behmanesh M. One-step synthesis of anionic peg-citrate G2 dendrimer and evaluation of its cytotoxicity in two cell lines. Pathobiol Res. 2015;17(4):13-24.
23. Khosravy MS, Shafiee Ardestani M, Ahangari Cohan R, Doroud D, Amini S, Momen SB, et al. Design, synthesis, physicochemical and immunological characterization of dendrimer-HBsAg conjugate. Vaccine Res. 2014;1(2):24-28.
24. Namazi H, Adeli M. Dendrimers of citric acid and poly (ethylene glycol) as the new drug delivery agents. Biomaterials. 2005;26(10):1175-1183.
25. Haririan I, Alavidjeh MS, Khorramizadeh MR, Ardestani MS, Ghane ZZ, Namazi H. Anionic linear-globular dendrimer-cis-platinum (II) conjugates promote cytotoxicity in vitro against different cancer cell lines. Int J Nanomed. 2010;5:63-75.
26. Mehrizi TZ, Ardestani MS. The introduction of dendrimers as a new approach to improve the performance and quality of various blood products (platelets, plasma and erythrocytes): a 2010-2022 review study. Curr Nanosci. 2023;19(1):103-122.
27. Derakhshan S, Shafiee Ardestani M, Zadeh Mehrizi T, Bitarafan-Rajabi A, Jokar S, Pirali Hamedani M, et al. (99m)Tc-SNW-1 nanoparticle labeling and its biodistribution/pathological evaluations. J Labelled Comp Radiopharm. 2025;68(9-10):e4160.
28. Ajdary N, Shafiee Ardestani M, Nequi Marnani H, Eshrati B, Zadeh Mehrizi T. Current strategies in the development of nanoformulations to enhance the stability of botox: a systematic review. AAPS PharmSciTech. 2025;27(1):38.
29. Rasoulianshiadehi M, Zadeh Mehrizi T, Eshrati B, Shafiee Ardestani M. Advances in targeted cancer imaging using galactose-modified polymeric nanoparticles: A systematic review. Iran J Nucl Med. 2026;34(1):32-47.
30. Mehrizi TZ, Mosaffa N, Hoseini MHM, Ardestani MS, Khamesipour A, Shahmabadi HE, et al. In vivo therapeutic effects of four synthesized antileishmanial nanodrugs in the treatment of leishmaniasis. Arch Clin Infect Dis. 2018;13(13):e80314.
31. Mehrizi TZ, Ardestani MS, Khamesipour A, Hoseini MHM, Mosaffa N, Anissian A, et al. Reduction toxicity of amphotericin b through loading into a novel nanoformulation of anionic linear globular dendrimer for improve treatment of leishmania major. J Mater Sci Mater Med. 2018;29(8):125.
32. Mehrizi TZ, Mirzaei M, Ardestani MS. Pegylation, a successful strategy to address the storage and instability problems of blood products: review 2011-2021. Curr Pharm Biotechnol. 2024;25(3):247-267.
33. Ray R, Ghosh S, Maity A, Jana NR. Arginine surface density of nanoparticles controls nonendocytic cell uptake and autophagy induction. ACS Appl Mater Interfaces. 2014;6(5):3451-5461.
34. Liu Y, Zou X, Portea-Manzano P, Fu J. Amino acid metabolism in breast cancer: pathogenic drivers and therapeutic opportunities. Protein Cell. 2025;16(7):506-531.
35. Prachenko EI, Bel'skaya LV. Transmembrane amino acid transporters in shaping the metabolic profile of breast cancer cell lines: the focus on molecular biological subtype. Curr Issues Mol Biol. 2024;47(1):4.
36. Song Y, Tang C, Yin C. Enhanced antitumor efficacy of arginine modified amphiphilic nanoparticles co-delivering doxorubicin and iSur-pDNA via the multiple synergistic effect. Biomaterials. 2018;150:1-13.
37. Sahoo RK, Nagori K, Naik B, Prusty D, Paliwal R, Gupta U. Poly-l-arginine grafted PAMAM dendrimers for the brain delivery of temozolomide in the management of glioblastoma multiforme: in-vitro and in-vivo evaluation. J Drug Deliv Sci Technol. 2025:107526.
38. Keshavarz A, Hajbabaei S, Sojoodi J, Saffari M, Afshar MAA, Monnavari F, et al. Mn2+ negatively charged pegylated dendrimer G2-tryptophan: Novel nano magnetic resonance imaging agent. Adv Appl Physiol. 2017;2:1-9.
39. Rasouli R, Zaaeri F, Rajabi AB, Darbandi-Azar A, Faridi-Majidi R, Ardestani MS. 99mTc-anionic linear globular dendrimer-G2-phenylalanine conjugate: novel brain tumor SPECT imaging. Biointerface Res Appl Chem. 2021;11(4):11244-11255.
40. Ajdary N, Davoudi M, Mehrizi TZ, Ardestani MS, Marnani HN, Shahmabadi HE, et al. Development and characterization of colloidally stable dendrimer–botox conjugates for targeted muscle delivery and radiolabeled imaging. Pharm Sci. 2026;32(2): 201-218.
41. Percie du Sert N, Hurst V, Ahluwalia A, Alam S, Avey MT, Baker M, et al. The ARRIVE guidelines 2.0: updated guidelines for reporting animal research. J Cereb Blood Flow Metab. 2020;40(9):1769-1777.
42. Varani M, Campagna G, Bentivoglio V, Serafinelli M, Martini ML, Galli F, et al. Synthesis and biodistribution

of 99mTc-labeled PLGA nanoparticles by microfluidic technique. Pharmaceutics. 2021;13(11):1769.
43. Maeda H, Nakamura H, Fang J. The EPR effect for macromolecular drug delivery to solid tumors: Improvement of tumor uptake, lowering of systemic toxicity, and distinct tumor imaging in vivo. Adv Drug Deliv Rev. 2013;65(1):71-79.
44. Kesharwani P, Puri V, Alqahtani T, Al Shmrany H, Gupta G, Goh KW, et al. PEGylated dendrimers for precision cancer therapy: advances in tumor targeting, drug delivery, and clinical translation. Biomater Adv. 2025;179:214493.
45. Tamtaji OR, Shafiee Ardestani M, Talebi Taheri A, Hamblin MR, Rahjoo T, Nabavizadeh F, et al. The effects of peptide IF7-conjugated dendrimer loaded with doxorubicin on colorectal cancer. Cancer Nanotechnol. 2025;16(1):11.
46. Ardestani MS, Hamedani MP, Ebrahimi SES, Mirzaei M, Khademian A, Ghoreishi SM. Synthesis and characterization of amlodipine-conjugated Gd3+-Citric acid PEG dendrimers for enhanced cardiac MRI contrast. J Mol Struct. 2025;1327:141236.
47. Kaveh Zenjanab M, Salemi A, Doustmihan A, Alimohammadvand S, Jahanban Esfahlan R. Dual-loaded niosome-dendrimer nanoplatform enhances Tirapazamine delivery to hypoxic breast cancer cells. Scientific Reports. 2025;15(1):29308.
48. Du X, Shi B, Liang J, Bi J, Dai S, Qiao SZ. Developing functionalized dendrimer-like silica nanoparticles with hierarchical pores as advanced delivery nanocarriers. Adv mater. 2013;25(41):5981-5985.
49. Zadeh Mehrizi T, Khamesipour A, Shafiee Ardestani M, Ebrahimi Shahmabadi H, Haji Molla Hoseini M, Mosaffa N, et al. Comparative analysis between four model nanoformulations of amphotericin B-chitosan, amphotericin B-dendrimer, betulinic acid-chitosan and betulinic acid-dendrimer for treatment of leishmania major: real-time PCR assay plus. Int J Nanomed. 2019;14:7593–760[illegible].
50. Hoo CM, Starostin N, West P, Mecartney ML. A comparison of atomic force microscopy (AFM) and dynamic light scattering (DLS) methods to characterize nanoparticle size distributions. J Nanopart Res. 2008;10(Suppl 1):89-96.
51. Cherkaoui S, Turn CS, Yuan Y, Lu W, Yang L, McBride MJ, et al. Reprogramming neuroblastoma by diet-enhanced polyamine depletion. Nature. 2025;646(8085):707-715.
52. Liu X, Ren B, Ren J, Gu M, You L, Zhao Y. The significant role of amino acid metabolic reprogramming in cancer. Cell Commun Signal. 2024;22(1):380.
53. Das SS, Das M, Pemmaraju DB. Nitric oxide synthase (NOS): the tactful diplomat in tumour-driven angiogenesis. Enzyme Based Approaches in Cancer Healthcare Management. Springer; 2026. 159-190.
54. Zaki Mahdi N. Investigation of the lethal effect of purified arginine deiminase purified from Lactobacillus plantarum p5 on murine mammary adenocarcinoma and vero cell lines. Arch Razi Inst. 2022;77(1):241-247.
55. Grimes JM, Khan S, Badeaux M, Rao RM, Rowlinson SW, Carvajal RD. Arginine depletion as a therapeutic approach for patients with covid-19. Int J Infect Dis. 2021;102:566-570.
56. Reid MS, Villalobos M, Cranston ED. The role of hydrogen bonding in non-ionic polymer adsorption to cellulose nanocrystals and silica colloids. Curr Opin Colloid Interface Sci. 2017;29:76-82.
57. Deschavannes A, Piquemal M, Rioufol C, Clotagatide A. Validation of an alternative two-strip method for the quality control of [99mTc] Tc-ETIFENIN (TECHIDA®). Appl Radiat Isot. 2025;217:111627.
58. Zhaoyun Y, Xiuzhen Q. Determination of radiochemical purity of 18F-fluorodeoxyglucose injection. J Isotopes. 2004;17(2): 104-107.
59. Cunnane CM, O'Brien LM, Waight LA, Millar AM. Determination of the radiochemical purity of (99m) Tc medronate injection by thin layer chromatography on iTLC-SG: effect of medronate concentration on the value measured. J Labelled Comp Radiopharm. 2013;56(5):301-304.
60. Bornholdt MG, Woolfenden M, Fang P, Jacobson MS, Hung JC. Rapid instant thin-layer chromatography system for determining the radiochemical purity of 68ga-tatate. J Nucl Med Technol. 2018;46(3):285-287.
61. You S, Han X, Xu Y, Yao Q. Research progress on the role of cationic amino acid transporter (CAT) family members in malignant tumors and immune microenvironment. Amino Acids. 2023;55(10):1213-1222.
62. Too CKL, Abdelmagid SA. l-arginine uptake and its role in the survival of breast cancer cells. l-arginine in clinical nutrition. Springer. 2016. 253-268.
63. Kashfi K, Kannikal J, Nath N. Macrophage reprogramming and cancer therapeutics: role of iNOS-derived NO. Cells. 2021;10(11):3194.
64. Hashempour Alamdari N, Alaei-Beirami M, Sadat Shandiz SA, Hejazinia H, Rasouli R, Saffari M, et al. Gd3+-asparagine-anionic linear globular dendrimer second-generation G2 complexes: novel nanobiohybrid theranostics. Contrast Media Mol Imaging. 2017;2017(1):3625729.
65. Khan MS, Alqahtani T, Al Shmrany H, Gupta G, Goh KW, Sahebkar A, et al. Enhanced permeability and retention (EPR) effect: advances in nanomedicine for improved tumor targeting. Biomater Adv. 2025;181:214636.
66. Deng X, Zhang Z, Ren T, Chen L. Regulation of oxidative stress and inflammation caused by drug accumulation in the TME based on EPR-passive strategy and active targeting. Cancer Nanotechnol. 2025;16(1):40.
67. Luthra K, Bhave A, Lele RD. Tc 99m sestamibi scanning in multiple myeloma--a new look with SPECT-CT. J Assoc Physicians India. 2014;62(9):801-812.
68. Mankoff DA, Dunnwald LK, Gralow JR, Ellis GK, Schubert EK, Charlop AW, et al. [Tc-99m]-sestamibi uptake and washout in locally advanced breast cancer are correlated with tumor blood flow. Nucl Med Biol. 2002;29(7):719-727.
69. Kobayashi M, Tsujiuchi T, Okui Y, Mizutani A, Nishi K, Nakanishi T, et al. Different efflux transporter affinity and metabolism of 99mTc-2-

methoxyisobutylisonitrile and 99mTc-tetrofosmin for multidrug resistance monitoring in cancer: Kobayashi et al. Pharm Res. 2019;36(1):18.
70. O'Connor MK, Morrow MMB, Hunt KN, Boughey JC, Wahner-Roedler DL, Conners AL, et al. Comparison of Tc-99m maraciclatide and Tc-99m sestamibi molecular breast imaging in patients with suspected breast cancer. EJNMMI res. 2017;7(1):5.
71. Okuda T, Kawakami S, Maeie T, Niidome T, Yamashita F, Hashida M. Biodistribution characteristics of amino acid dendrimers and their pegylated derivatives after intravenous administration. J Control Release. 2006;114(1):69-77.
72. Medina SH, Tiruchinapally G, Chevliakov MV, Durmaz YY, Stender RN, Ensminger WD, et al. Targeting hepatic cancer cells with pegylated dendrimers displaying N-acetylgalactosamine and SP94 peptide ligands. Adv Healthc Mater. 2013;2(10):1337-1350.
73. Zheng K, Ouyang X, Xie H, Peng S. Responsive zwitterionic materials for enhanced drug delivery. Langmuir. 2025;41(6):3744-3756.
74. Du B, Jiang X, Das A, Zhou Q, Yu M, Jin R, et al. Glomerular barrier behaves as an atomically precise bandpass filter in a sub-nanometre regime. Nat Nanotechnol. 2017;12(11):1096-1102.
75. Naumenko V, Nikitin A, Kapitanova K, Melnikov P, Vodopyanov S, Garanina A, et al. Intravital microscopy reveals a novel mechanism of nanoparticles excretion in kidney. J Control Release. 2019;307:368-378.
76. Peracchia MT, Fattal E, Desmaele D, Besnard M, Noel JP, Gomis JM, et al. Stealth® pegylated polycyanoacrylate nanoparticles for intravenous administration and splenic targeting. J Control Release. 1999;60(1):121-128.
77. Orsini F, Puta E, Guidoccio F, Mariani G. Single-photon-emitting radiopharmaceuticals. nuclear medicine textbook: methodology and clinical applications. Springer. 2019. 21-56.
78. Hays MT, Berman M. Pertechnetate distribution in man after intravenous infusion: a compartmental model. J Nucl Med. 1977;18(9):898-904.
79. Yan X, Lin L, Li S, Wang W, Chen B, Jiang S, et al. Arginine-rich peptide based nanoparticles with bridge-like structure: Enhanced cell penetration and tumor therapy effect. Chem Eng J. 2020;395:125171.
80. Kostryukova LV, Tereshkina YA, Bedretdinov FN, Gisina AM. The effect of addition of two targeted vectors, cRGD peptide and folic acid, with the same linker length on the properties of the doxorubicin phospholipid composition: a study of properties in vitro. Biomed Khim. 2025;71(1):37-50.
81. Davoudi M, Jadidi Y, Moghaddam F Farrokhi V, Afrisham R. Ameliorative impacts of polymeric and metallic nanoparticles on cisplatin-induced nephrotoxicity: a 2011–2022 review. J Nanobiotechnology. 2022;20(1):504.
82. Vorster M, Sathekge M. 18F-FDG PET/CT for prediction of response in breast cancer. Semin Nucl Med. 2026;56(1):86-96.
83. Collarino A, Pisano G, Hruska CB, Garganese G, Fowler AM, Florit A, et al. Current and future perspectives of molecular breast imaging with [99mTc] Tc-Sestamibi: An IAEA international expert panel. Eur J Nucl Med Mol Imaging. 2026;53(7):4348-4359.